Pergamon

Acta mater. 49 (2001) 2567–2582

Acta MATERIALIA

www.elsevier.com/locate/actamat

ANALYTICAL AND COMPUTATIONAL DESCRIPTION OF EFFECT OF GRAIN SIZE ON YIELD STRESS OF METALS

H. -H. FU, D. J. BENSON and M. A. MEYERS†

Dept. of Mechanical and Aerospace Engineering, University of California, San Diego, Mail Code 0411, 9500 Gilman Drive, La Jolla, CA 92093, USA

(Received 28 July 2000; received in revised form 22 January 2001; accepted 22 January 2001)

Abstract—Four principal factors contribute to grain-boundary strengthening: (a) the grain boundaries act as barriers to plastic flow; (b) the grain boundaries act as dislocation sources; (c) elastic anisotropy causes additional stresses in grain-boundary surroundings; (d) multislip is activated in the grain-boundary regions, whereas grain interiors are initially dominated by single slip, if properly oriented. As a result, the regions adjoining grain boundaries harden at a rate much higher than grain interiors. A phenomenological constitutive equation predicting the effect of grain size on the yield stress of metals is discussed and extended to the nanocrystalline regime. At large grain sizes, it has the Hall–Petch form, and in the nanocrystalline domain the slope gradually decreases until it asymptotically approaches the flow stress of the grain boundaries. The material is envisaged as a composite, comprised of the grain interior, with flow stress σ_{fG}, and grain boundary work-hardened layer, with flow stress σ_{fGB}. The predictions of this model are compared with experimental measurements over the mono, micro, and nanocrystalline domains. Computational predictions are made of plastic flow as a function of grain size incorporating differences of dislocation accumulation rate in grain-boundary regions and grain interiors. The material is modeled as a monocrystalline core surrounded by a mantle (grain-boundary region) with a high work hardening rate response. This is the first computational plasticity calculation that accounts for grain size effects in a physically-based manner. A discussion of statistically stored and geometrically necessary dislocations in the framework of strain-gradient plasticity is introduced to describe these effects. Grain-boundary sliding in the nanocrystalline regime is predicted from calculations using the Raj–Ashby model and incorporated into the computations; it is shown to predispose the material to shear localization.

Keywords: Nanocrystalline materials; Grain size; Hall–Petch

1. INTRODUCTION

The grain-size dependence of yield stress in metals has been represented as a $D^{-1/2}$ relationship since the pioneering work of Hall [1] and Petch [2]. The term Hall–Petch was introduced by Conrad and Schoeck [3] as a tribute to these researchers. The original explanation for this effect, envisaged by Hall and Petch, was that pile-ups formed at grain boundaries, and required a critical stress to break through them. This was followed by Cottrell [4], who suggested a more realistic scenario; that the stress concentration due to pile-ups activated sources in the surrounding grains. Armstrong [5] presents a critical overview of the effects. Departures of this pile-up scenario were proposed by Li [6] and Conrad [7] who invoked grain-boundary dislocation sources and a grain-size dependence of dislocation density, respectively. The important contributions by Ashby [8], Hirth [9], and Thompson [10] further strengthened the argument that causes other than pile-ups were responsible for the grain size effects. Clear evidence for the formation of a layer of high dislocation density in the direct vicinity of the grain boundaries, starting at an applied stress below the global yield stress, is the transmission electron microscopy by Murr and Hecker [11] (especially, Fig. 2). In similar experiments in Fe–3%Si, Suits and Chalmers [12], and Worthington and Smith [13] incontrovertibly demonstrated that stresses are higher in the grain-boundary region than in the grain interiors. This was corroborated by Margolin and Stanescu [14] for β titanium. Meyers and Ashworth [15] proposed a mechanism based on elastic anisotropy of the grains. Nevertheless, pile-ups are still widely recognized as the dominating effect.

The Hall–Petch relationship has recently come under close scrutiny in the context of nanocrystalline materials pioneered by Gleiter and coworkers [16, 17]. Weertman and coworkers [18–21] have investi-

† To whom all correspondence should be addressed. Tel.: +1-858-534-4719; fax: +1-858-534-5698

E-mail address: mameyers@mae.ucsd.edu (M. A. Meyers)

1359-6454/01/$20.00 © 2001 Published by Elsevier Science Ltd on behalf of Acta Materialia Inc.
PII: S1359-6454(01)00062-3

gated the effect of grain size, in the nanocrystalline domain, on yield stress, in a systematic manner. Sample imperfections (voids, microcracks incomplete boundary of particles) masked many of the mechanical characteristics of nanocrystalline materials in early work, and careful processing and characterization has been needed to eliminate (or, at least, mitigate) these effects. A recent overview [21] presents the current thinking on this. Several mechanisms explaining the strength of nanocrystalline metals have been advanced. In one school of thought, Armstrong and coworkers [22–24] calculated the minimum size of a pile-up and concluded that pile-ups cannot be responsible for the yield stress-grain size effects in the nanocrystalline regime. Koch and coworkers [25–29] studied nanocrystalline iron; a focused effect was also undertaken to remove flaws (voids, microcracks, incomplete boundaries of particles, etc.) in order to obtain more reliable mechanical strength under both compression and tension. In summary, the experimental results indicate that the Hall–Petch slope in the nanocrystalline domain is lower than in the microcrystalline (conventional) range of grain sizes. In some cases, a zero or even negative Hall–Petch slope has been reported [30]; however, this may well be an artifact of sample preparation.

An attractive approach to the analytical prediction of the grain-size dependence is through strain-gradient plasticity. Strain-gradient plasticity is a recent development that incorporates a length scale in the analytical treatment of plasticity problems. It enables the prediction of the effect of indentation size on the hardness of metals and ceramics, the effect of hard particles in the work hardening of metals, grain size, and other effects. Originally proposed by Aifantis [31] in the context of shear localization, it has been extended to a variety of problems by Fleck *et al*. [32, 33] and Gao *et al*. [34, 35]. From the dislocation perspective, the evolution of statistically stored and geometrically necessary dislocations, first proposed by Ashby [8], provides the underlying physics. The physical processes envisaged for the grain-size dependence of yield and flow stresses involve a length scale. Fleck *et al*. [32, 33] apply the geometrically necessary (ρ_g) and statistically stored (ρ_s) dislocation densities to determine the athermal component of the flow stress, through the conventional Taylor expression:

$$\tau_\mu = \alpha G b(\rho_g + \rho_s)^{1/2} \tag{1}$$

where α is a geometrical factor, G is the shear modulus and b the Burgers vector. The evolution of ρ_s and ρ_g is affected by both γ and $d\gamma/dl$ (γ is the shear strain and l is a length scale), which determine the mean free path, λ. Thus, they arrive at (the thermal component of τ, τ^*, is assumed to be independent of grain/obstacle size):

$$\tau = \tau^* + \tau_\mu = \tau^* + \alpha G b\left(\frac{\chi_e}{b} + \frac{\varepsilon_p^2}{\lambda_{II} b}\right)^{1/2} \tag{2}$$

where χ_e is a scalar measure of curvature and ε_p is the effective plastic strain; λ_{II} is the work hardening rate in Stage II (linear hardening). χ_e is directly related to the strain gradient, $d\gamma/dl$. The length scale, l, can be taken as the grain size, D, or a fraction thereof.

This theoretical framework does not incorporate the formation of a grain boundary work-hardened layer. Furthermore, it does not predict a grain-size dependence of yield stress, since both the curvature and plastic strain are zero prior to plastic deformation. As work hardening builds up, the effect manifests itself, resulting in an increased work hardening for decreasing grain size. It is the objective of this paper to provide some additional insights.

2. ELASTIC ANISOTROPY

A polycrystalline aggregate, upon being subjected to external tractions, develops a highly inhomogeneous state of internal stresses, due to the elastic anisotropy of the individual grains. For elastic deformations, such inhomogeneous state of stress can only be avoided if the anisotropy ratio, A, is one. For instance, for iron and copper, one has:

Fe	Cu
E_{100}=125 GPa	E_{100}=67 GPa
E_{110}=200 GPa	E_{110}=130 GPa
E_{111}=272 GPa	E_{111}=190 GPa
A=2.43	A=3.21

Figure 1 shows polar plots of Young moduli for monocrystalline iron and copper. The effect of orientation on E is revealed in a striking manner. This is a well known but often ignored effect. This anisotropy generates additional stresses in the regions adjoining the grain boundaries. Figure 2 shows a polycrystalline aggregate subjected to compressive tractions through the uniform displacement of the end platens. The computational approach is described in Section 5. The average imposed stress, obtained by multiplying the strain (set equal to 2.25×10^{-4}) by the polycrystalline Young's modulus (120 GPa), is equal to 27.9 MPa. The arrangement of grains is shown in Fig. 2(a). Three types of grains, with orientations [100], [110], and [111], with respect to the loading axis, are considered. They are white, gray, and black, respectively, in Fig. 2(a). The material is not truly anisotropic, because the individual grains are taken to be isotropic, (but with different Young moduli). Fig. 2(b) and (c) show the principal stresses σ_1 and σ_2, and their variation through the section marked A–A. As expected, σ_1 fluctuates around zero, where σ_2 varies between -20 and -55 MPa. The maximum shear stress is shown in Fig. 2(d). It varies between 13 and 30 MPa. The stresses are seen to vary significantly throughout

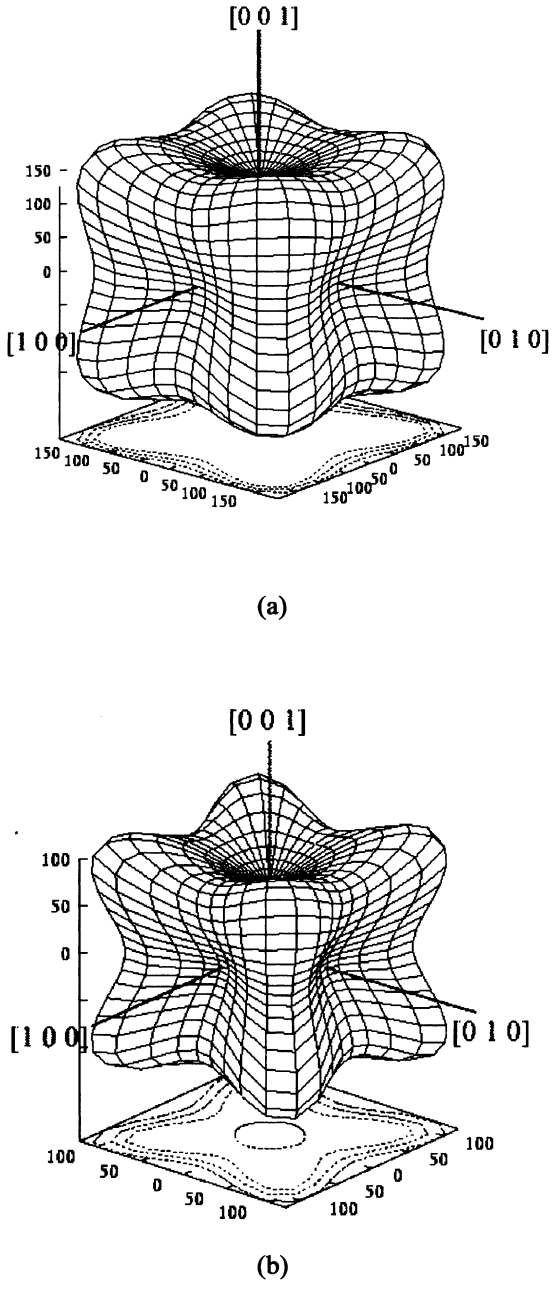

Fig. 1. Polar plots of E showing elastic anisotropy in (a) iron and (b) copper.

the grains. The maximum shear stress in a homogeneous material would have a value of 20 MPa at the applied displacement. Ghahremani *et al*. [36] and Ghahremani and Shih [37] carried out analytical calculations of anisotropy effects and found that singularities exist at the grain-boundary vertices (stress proportional to r^{-s}, where $s>1/2$) that can be stronger than crack singularities. These singularities are, of course, dependent on the anisotropy ratio A. It can be concluded that elastic stresses vary considerably in polycrystalline aggregates.

3. ANALYTICAL TREATMENT

3.1. Phenomenological model

A mechanism for the effect of grain size on the yield stress is presented here. It is essentially an extension of the model proposed by Meyers and Ashworth [15] to the nanocrystalline regime. This model does not require pile-ups at grain boundaries. It is based on earlier ideas advanced by Ashby [8], Hirth [9], and Thompson [10]. Conceptually, it is supported by and parallel to ideas developed by Margolin [38]. It will be shown that the Meyers–Ashworth (MA) model, which has a built-in deviation from a Hall–Petch relationship at small grain sizes, can be successfully extended to the nanocrystalline regime. The concept of a work-hardened grain-boundary layer, essential to the MA model, is modeled computationally in Section 5.2, for different grain sizes, and it is shown that similar predictions are obtained. The compatibility requirement at the grain boundaries creates additional stresses, τ_I. Meyers and Ashworth [15] found for nickel that

$$\tau_I = 1.37\sigma_{AP} \tag{3}$$

where σ_{AP} is the applied normal stress. In a uniform, homogeneous material, the maximum shear stress is $\tau = \sigma/2$. Thus, the shear stress at the interface is between 2 and 3 times the maximum shear stress in a homogeneous/uniform material. This is consistent with the result given in Section 2 for copper. It is therefore logical to expect the initiation of plastic flow to take place in the grain-boundary regions. Other factors that contribute to this are:

1. Grain boundaries are sources of dislocations. This is a well-known phenomenon; grain-boundary ledges and grain-boundary dislocations can initiate plastic deformation (e.g., Li and Chou [39], Murr [40], Sutton and Balluffi [41]).
2. Grain boundaries segregate impurities and foreign atoms, and their mechanical properties differ from the grain interiors.
3. Dislocations pile up at grain boundaries.

As a result, while the grain interiors can be considered to harden by the classic easyglide/linear hardening/parabolic hardening sequence, the grain boundaries show a much faster rise in dislocation density and hardening rate. This is exemplified by the results shown by Hirth [9] for a bicrystal. Although this is a compatible bicrystal, the activation of a second slip system around the boundary is seen. This conceptual frame is extended to a polycrystal in Fig. 3(b). The grain-boundary regions are shown with pronounced slip activity on two slip systems; this leads to a much higher hardening rate than the grain interiors. Recent results on copper polycrystals [42]

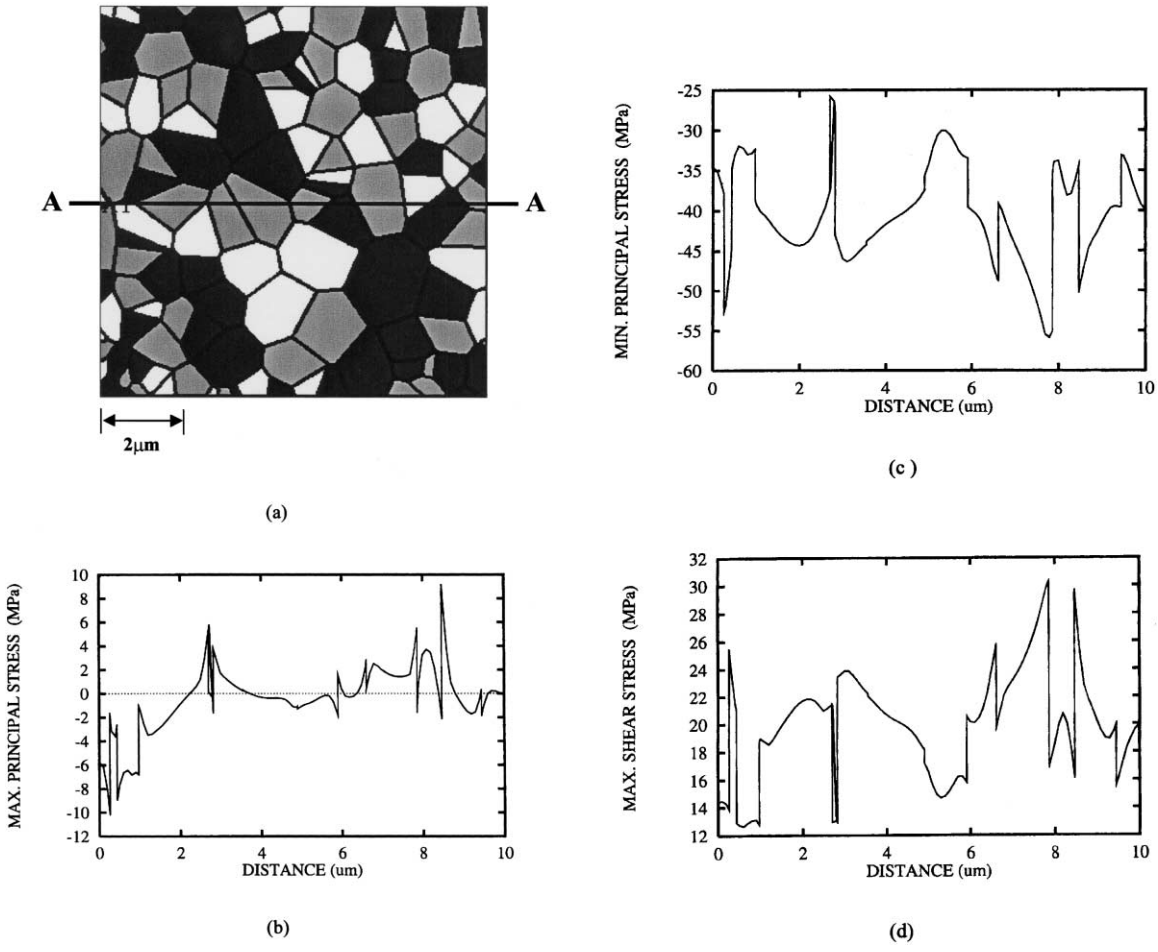

Fig. 2. Elastic stresses in polycrystalline copper loaded elastically; (a) grain configuration; three grain orientations white [100], gray [110], and black [111]; (b) maximum principal stress (σ_1); (c) minimum principal stress (σ_2); (d) maximum shear stress.

show a much greater tendency for slip on two or three systems in the regions close to the boundaries. It is of note that grain-boundary corners are regions especially prone to concentrated plastic deformation. Recent results by Gray *et al.* [43] confirm the higher hardening in the regions adjacent to grain boundaries and triple points. This serves as a basis for the model developed by Meyers and Ashworth [15].

The model is presented here in a shortened manner. Figure 4 shows the sequence of stages as the applied stress, σ_{AP}, is increased. As the applied stress increases, a work hardened layer along the grain boundaries is formed. This is eloquently illustrated by Murr and Hecker [11]. This build-up of plastic deformation has also been recently measured by Adams and King [44]. The use of electron backscattering diffraction in orientation imaging microscopy of an aluminum bicrystal deformed to a strain of 0.1 revealed a significantly higher dislocation density (as inferred from the distortion measurements) in the vicinity of the grain boundary. Once this work hardened grain-boundary layer is formed, the stresses within the polycrystalline aggregate homogenize. Stages a–c in Fig. 4 represent the dominance of elastic compatibility strains and the formation of a grain boundary work-hardened layer. Stages d–f represent the response of a composite material, consisting of dislocation-free grain interiors, with a flow stress σ_{fG}, and grain-boundary layers, with a flow stress σ_{fGB}. The flow stress of the grain aggregate is obtained, in approximate fashion, from:

$$\sigma_y = A_G\sigma_{fG} + A_{GB}\sigma_{fGB}. \tag{4}$$

A_G and A_{GB} are the areal fraction of grain interior and grain boundary, respectively. Figure 5 shows an idealized representation of the aggregate. Grains are assumed to be spherical, with a diameter D; the grain boundary layers are assumed to have a thickness t (in each grain, $t<D/2$).

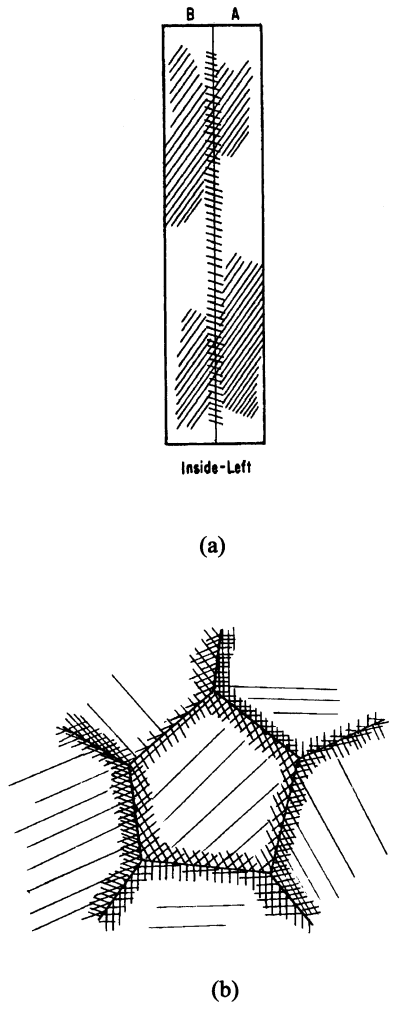

Fig. 3. (a) Activation of slip on second system in the vicinity of boundary due to compatibility stresses in Fe–3% Si (from Hirth [9]:3047); (b) Generalization for polycrystalline aggregate.

The diametral areal fractions are expressed by:

$$A_{GB} = \frac{\frac{1}{4}\pi[D^2-(D-2t)^2]}{\frac{1}{4}\pi D^2} = 4\left[\frac{t}{D}-\left(\frac{t}{D}\right)^2\right], \quad (5)$$

$$A_G = \frac{\frac{1}{4}\pi(D-2t)^2}{\frac{1}{4}\pi D^2} = 1-A_{GB}. \quad (6)$$

Substituting equation (5) and (6) into (4)

$$\sigma_y = \sigma_{fG} + 4(\sigma_{fGB}-\sigma_{fG})tD^{-1}-4(\sigma_{fGB}-\sigma_G)t^2D^{-2} \quad (7)$$

Different sections, marked S_1, S_2, S_3, S_4, and S_5 in Fig. 5(b), produce different areal fractions A_G and A_{GB}. Hence, it is more correct to use the mean values of t and D, $\bar{t}$ and $\bar{D}$, respectively, so that:

$$\sigma_y = \sigma_{fG} + 4(\sigma_{fGB}-\sigma_{fG})\bar{t}\,\bar{D}^{-1} -4(\sigma_{fGB}-\sigma_G)\bar{t}^2\bar{D}^{-2} \quad (8)$$

Meyers and Ashworth [15] estimated these mean values. They are:

$$\bar{D} = \frac{\pi}{4}D,\ \bar{t} = 1.57t. \quad (9)$$

The term $\bar{t}\bar{D}^{-1}$ is approximately equal to $2tD^{-1}$ and equation (8) becomes:

$$\sigma_y = \sigma_{fG} + 8(\sigma_{fGB}-\sigma_{fG})tD^{-1} -16(\sigma_{fGB}-\sigma_G)t^2D^{-2} \quad (10)$$

The variation of the thickness t of the work hardened grain-boundary layer has to be considered. There are two effects: (a) as the grain size is decreased, the stress field fluctuations vary with D. This would lead to a dependency $t=k_1D$; (b) the dislocation spacing is unchanged and the dislocation interactions will dictate a constancy in t; thus, a relationship $t=k_2D^0$. The geometric mean would be: $(k_1k_2D)^{1/2}$. This produces the expected Hall–Petch dependence, as is shown below. Hence:

$$t = (k_1k_2D)^{1/2} = k_{MA}D^{1/2} \quad (11)$$

Substituting equation (11) into equation (10),

$$\sigma_y = \sigma_{fG} + 8k_{MA}(\sigma_{fGB}-\sigma_{fG})D^{-1/2} -16k_{MA}^2(\sigma_{fGB}-\sigma_{fG})D^{-1} \quad (12)$$

For large grain sizes (the micrometer range) the $D^{-1/2}$ term dominates and a Hall–Petch relationship is obtained. The Hall–Petch slope, k_{HP}, is equal to:

$$k_{HP} = 8k_{MA}(\sigma_{fGB}-\sigma_{fG}) \quad (13)$$

As the grain size is decreased, the D^{-1} term becomes progressively dominant, and the σ_y vs. $D^{-1/2}$ curve goes through a maximum. This occurs at:

$$D_c = (4k_{MA})^2. \quad (14)$$

For values of $D<D_c$, it is assumed that the flow stress reaches a plateau and that grain-boundary effects dominate plastic flow.

3.2. Work hardening

The strain gradient theory does not take into consideration the difference in dislocation density observed between the grain interiors and the grain boundary regions. A framework incorporating the strain gradient concepts and more attuned to the physics of the problem would be to track the dislo-

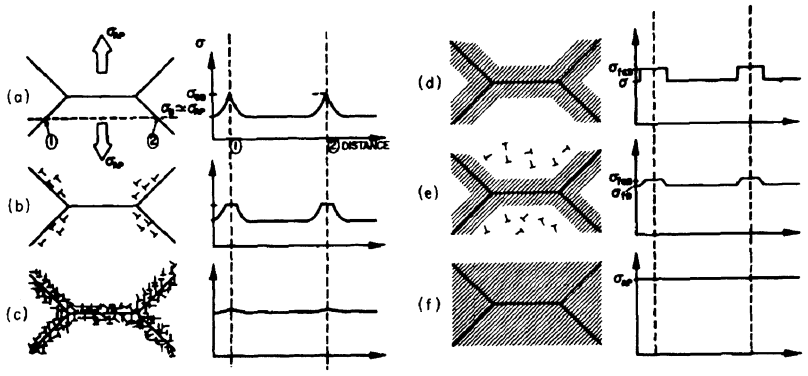

Fig. 4. Sequence of stages in polycrystalline deformation, starting with (a, b) localized plastic flow in the grain-boundary regions (microyielding), forming a grain-boundary work-hardened layer (c, d) that effectively reinforces the microstructure, and leading to (e, f) macroyielding in which the bulk of the grains undergo plastic deformation. (from Meyers and Ashworth [15]).

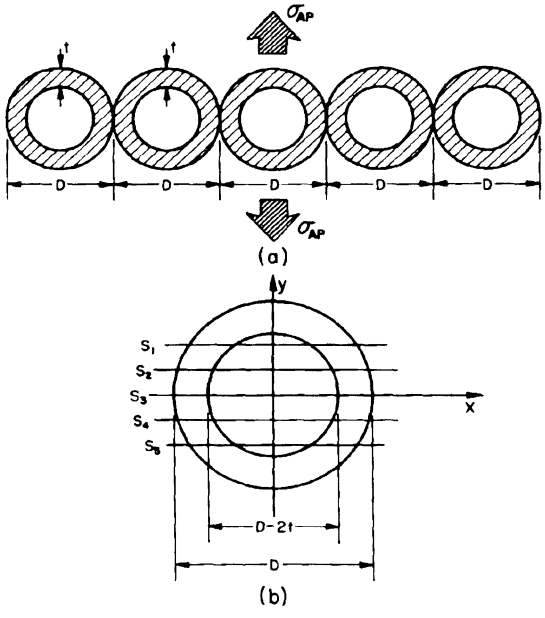

Fig. 5. (a) Polycrystalline aggregate viewed as composite material composed of bulk and grain-boundary material, with flow stresses σ_{GB} and σ_{fGB} respectively. (b) Idealized spherical grain of diameter D with grain-boundary layer of thickness t; sections S_1, S_2, S_3, S_4, and S_5, reveal different proportions between the areas of the bulk and grain-boundary material. (from Meyers and Ashworth [15].)

cation densities in both grain interior and boundary. We will use the approach developed by Klepaczko [45], which consists of considering the dislocation accumulation rate as the sum of a multiplication rate and an annihilation rate. For the grain-boundary region:

$$\frac{d\rho_{GB}}{d\gamma} = M_{GB} - N_{GB}(\rho_{GB} - \rho_0). \tag{15}$$

M_{GB} and N_{GB} are dislocation multiplication and annihilation rates, respectively. Dislocations are annihilated at an increasing rate, as their density increases. Klepaczko [45] took a linear increase, starting with a threshold density ρ_0. This occurs primarily by dynamic recovery.

A similar equation to equation (15) can be developed for the grain interior,

$$\frac{d\rho_G}{d\gamma} = M_G - N_G(\rho_G - \rho_0). \tag{16}$$

For the grain interior, one has to consider the significantly different values of M_G and N_G. There are two stages: easy glide and linear/parabolic hardening. An expression that incorporates these effects is

$$\frac{d\rho_G}{d\gamma} = H(\rho_0^{II} - \rho_G)M_G^I + H(\rho_G - \rho_0^{II}) \\ [M_G^{II} - N_G^{II}(\rho_G - \rho_0^{II})]. \tag{17}$$

M_G^I and M_G^{II} are multiplication rates for stages I (easy glide) and II (linear/parabolic hardening), N_G^{II} is the annihilation rate for stage II and $H(\rho_G - \rho_0^{II})$ is a Heaviside function that "turns on" at the beginning of stage II. It is assumed that in stage I there is no dislocation annihilation, because of their relatively low density ($N_G^I = 0$ for $\rho_0^I \leq \rho_G \leq \rho_0^{II}$).

Solving equation (15):

$$\gamma = \int_{\rho_0}^{\rho_{GB}} \frac{d\rho_{GB}}{M_{GB} - N_{GB}(\rho_{GB} - \rho_0)} + C_1 \tag{18}$$

$$\gamma = -\frac{1}{N_{GB}} \ln \frac{M_{GB} - N_{GB}(\rho_{GB} - \rho_0)}{M_{GB}} + C_1 \tag{19}$$

Using the boundary condition ($\gamma = 0, \rho_{GB} = \rho_0$), $C_1 = 0$. Thus,

$$\rho_{GB} = \rho_0 + \frac{M_{GB}}{N_{GB}}(1 - e^{-N_{GB}\gamma}). \tag{20}$$

From equation (17):

$$\gamma = \int_{\rho_0^I}^{\rho_G} \frac{d\rho_G}{H(\rho_0^{II}-\rho_G)M_G^I + H(\rho_G-\rho_0^{II})[M_G^{II}-N_G^{II}(\rho_G-\rho_0^{II})]}. \tag{21}$$

Thus, in stage I,

$$\gamma = \frac{\rho_G-\rho_0^I}{M_G^I}, \tag{22}$$

while in stage II,

$$\gamma = \int_{\rho_0^I}^{\rho_0^{II}} \frac{d\rho_G}{M_G^I} + \int_{\rho_0^{II}}^{\rho_G} \frac{d\rho_G}{M_G^{II}-N_G^{II}(\rho_G-\rho_0^{II})} \tag{23}$$

$$\gamma = \frac{1}{M_G^I}(\rho_0^{II}-\rho_0^I) - \frac{1}{N_G^{II}}\ln\frac{M_G^{II}-N_G^{II}(\rho_G-\rho_0^{II})}{M_G^{II}} \tag{24}$$

Assuming an iso-strain configuration (which is a good approximation in the plastic regime) during plasticity and applying the Taylor equation:

$$\tau = \alpha G b(V_G\rho_G + V_{GB}\rho_{GB})^{1/2} \tag{25}$$

One can obtain a τ vs. γ relationship by inserting equation (19) and equation (24) (after inversion) into equation (25). The volume fraction V_{GB}, on its turn, can be expressed as a function of grain size, D, by means of equation (11).

4. COMPARISON WITH EXPERIMENTS

The predictions of equation (12) are compared with the most extensive experimental results available in the literature, to the authors' knowledge. Yield stresses for nanocrystalline Fe and Cu, reported by Mallow and Koch [27], and Weertman *et al*. [21], respectively, are shown in Fig. 6. Hall–Petch slopes in the microcrystalline range complement the experimental results in the nanocrystalline range. These slopes are reported in the literature. For iron, experimental results reported by Armstrong [5] were used. For copper, experimental results by Feltham and Meakin [46] and Andrade *et al*. [47] are used. There are other experimental results in the literature, that fall in the range reported in Fig. 6. For iron, Abrahamson [48] carried out experiments in the lower range of the conventional Hall–Petch and started to observe a deviation from the accepted slope. Two experimental points from Abrahamson [48] are shown in Fig. 6(a); the Hall–Petch slope starts to decrease.

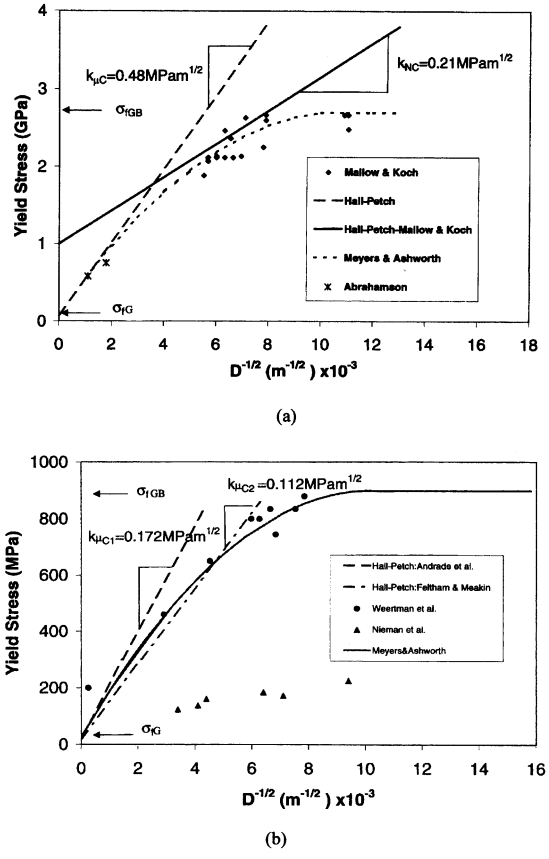

Fig. 6. σ_y vs. $D^{-1/2}$ relationship for (a) iron and (b) copper; comparison of experimental results and predictions of equation (12).

It is clear, for both Fe and Cu, that the σ_y vs. $D^{-1/2}$ relationship is not linear over the entire mm–nm range. The Hall–Petch line is an approximation that is effective in the mm–μm range. There is strong evidence that the slope decreases and that the curve asymptotically approaches a plateau when the grain size is progressively reduced. Equation (12) is successful in representing the principal features experimentally observed. Three parameters have to be established: σ_{fG}, σ_{fGB}, and k_{MA}. σ_{fGB} is the saturation stress and represents the flow stress of the work hardened grain-boundary layer. It is taken as the maximum of the yield stress. k_{MA} is obtained by conversion of k_{HP} according to equation (13). This ensures a good match between HP and MA for large grain sizes. Table 1 shows the parameters used in the calculation. The continuous curves in Fig. 6 represent the application of equation (12); a reasonable fit is obtained and the principal features are captured. For grain sizes below the maximum of the flow stress in the MA equation, a straight horizontal line is taken; in this regime, the grain boundaries (σ_{fGB}) dominate the process.

Table 1. Parameters used for MA model

	σ_{fG} (MPa)	σ_{fGB} (MPa)	k_{HP} (MPa $m^{1/2}$)	k_{MA} ($m^{1/2}$)
Fe	100	2800	0.48	2.2×10^{-5}
Cu	25	900	0.112–0.172	$(1.6–2.4)\times10^{-5}$

There are many simplifications and assumptions in this model. The most prominent are:

1. The work hardened layer t is assumed to have a grain size dependence of $D^{-1/2}$. This assumption is based on the σ_y vs. $D^{-1/2}$ dependence.
2. The flow stress of this layer is constant. In reality, a gradient of work hardening is expected.
3. The grain boundary flow stress reaches the saturation value σ_{fGB} at an early level of global plastic strain.

In spite of these drastic assumptions, a good fit is obtained and it is felt that the model captures the key physical features. It should be noted that Gertsman *et al*. [49] obtained experimentally a similar decrease in the Hall–Petch slope for copper, in the nanocrystalline range. However, the yield stresses are significantly lower than the latest results by Weertman *et al*. [20, 21]. Differences can be attributed to improved processing methods. Figure 6(b) also shows (▲) earlier experimental data by Nieman *et al*. [18]. These results illustrate how much processing can affect the strength of nanocrystalline materials. These results were not used in the modeling effort.

5. COMPUTATIONAL PREDICTIONS

5.1. Description of code

The finite difference community has used Eulerian methods for over thirty years to analyze problems with explosive loading, but until comparatively recently, they were too computationally demanding and inaccurate to be attractive for solving problems in solid mechanics. The strengths and weaknesses of the Eulerian formulation are summarized in a brief description of the computational methods used in *Raven*, an explicit, multi-material Eulerian program developed by Benson. A comprehensive review paper by Benson [50] discusses the algorithms in greater detail.

Operator splitting replaces a differential equation with a set of equations that are solved sequentially. This strategy is formally limited to second order accuracy [50], which is achieved in practice. While the first strategy does not have this theoretical limitation, it rarely achieves better than first order accuracy in multi-material formulations.

A generic transport equation is

$$\frac{\partial \varphi}{\partial t} + \vec{u}\cdot\nabla\varphi = \Phi \tag{26}$$

where φ is a solution variable, $\vec{u}$ is the velocity, and Φ is a source term. This equation is split into

$$\frac{\partial \varphi}{\partial t} = \Phi \tag{27}$$

$$\frac{\partial \varphi}{\partial t} + \vec{u}\cdot\nabla\varphi = 0 \tag{28}$$

where equations (27) and (28) are referred to as the Lagrangian and Eulerian steps respectively. The Lagrangian step uses the central difference algorithm to advance the solution in time in the same manner as a standard explicit Lagrangian finite element formulation.

The elements are four-node quadrilaterals with one-point integration and a viscous hourglass control. Hourglass modes may stop Lagrangian calculations performed with uniformly reduced integration by turning the elements inside out. Since the hourglass modes are orthogonal to the strain field, the stresses in the elements are unaffected by the modes. The Eulerian formulation is immune to the mesh distortion problem, but the hourglass viscosity is included to filter out the diamond pattern the hourglass modes introduce into the contours of the velocity field.

The transport calculation is equivalent to a projection of the solution from one mesh onto another, and a perfect projection should be completely conservative. Most transport algorithms are conservative by construction: a flux added to one element is subtracted from its neighbor.

Van Leer [51] developed the MUSCL transport algorithm used in the current calculation. The transport volumes are geometrical calculations defined by the mesh motion and they are independent of the transport kernel. The one-dimensional algorithm is extended to two dimensions by performing sweeps along one mesh direction, then another sweep in the other direction.

5.2. Results of computations

For computational calculations, realistic polycrystals were used and are shown in Fig. 7. Five grain sizes were modeled: 100, 10, 1, and 0.1, 0.05 (50 nm), and 0.026 (26 nm) μm. The last grain size was selected to model the results by Weertman *et al*. [21]. The material chosen for the modeling effort is copper, because of the significant amount of information on grain-size effects available (see Fig. 6(b)). The micro-

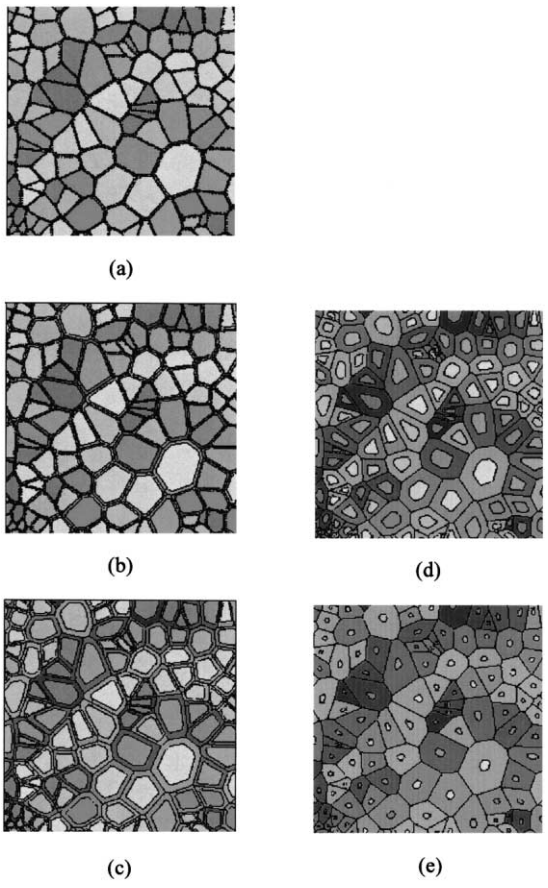

Fig. 7. Simulated polycrystalline aggregate used in computations; (a) D=100 μm, t=3.33 μm; (b) D=10 μm, t=0.665 μm; (c) D=1 μm, t=0.133 μm; (d) D=0.1 μm, t=0.0265 μm; (e) D=0.026 μm, t=0.0103 μm.

structures, already divided into grain interiors and grain-boundary layers, are shown in Fig. 7. For the largest grain size modeled (100 μm), the grain-boundary region is barely distinguishable, whereas for the smallest grain size (0.026 μm), the grain-boundary region occupies a significant portion of the entire grain. The following relationship, diverging slightly from the $D^{1/2}$ form of equation (11), was chosen:

$$t(\text{in } \mu\text{m}) = 0.133D^{0.7} \tag{29}$$

The different mechanical responses of the two regions were also incorporated. The grain-boundary region was considered to harden at a high rate, whereas the grain interiors were modeled as monocrystals. The model has the capability of incorporating as many as fifteen different crystallographic directions (manifested by different mechanical responses). This is indicated by the different colors in Fig. 7, each color representing a grain with a unique mechanical response. However, at the present stage the grain interiors were assumed to have only three different (monocrystalline) responses. The crystallographic orientation and specimen dimensions have a profound effect on the mechanical response of copper monocrystals. The various points on the stereographic triangle of Fig. 8 represent orientations of monocrystals tested by Diehl [52]. Three crystallographic orientations are circled in Fig. 8: C23, C26, and C30. They were used in the computations. They represent a soft, a medium, and a hard orientation. The respective elastic moduli are also shown. Each grain was considered isotropic, but having its own Young's modulus. The "effective" elastic moduli were calculated from the direction cosines for the crystallographic orientations and the compliances S_{ij}. The monocrystal stress–strain responses are taken from results reported by Diehl [52] and extended from a best fit with data for larger strains using results from Suzuki *et al.* [53]; this was necessary because the results from Diehl [52] do not extend to the strain range required in the computations. The corresponding stress–strain curves, for the orientations C23, C26, and C30, are shown in Fig. 9(a).

The more rapidly work-hardening grain-boundary region was assumed to respond by a Voce equation [54]:

$$\frac{\sigma_s-\sigma}{\sigma_s-\sigma_0} = \exp\left(-\frac{\varepsilon}{\varepsilon_c}\right) \tag{30}$$

Three parameters define the mechanical response: σ_0, the initial yield stress; σ_s, the saturation stress, and ε_c, a characteristic strain. Kocks [55] discusses the advantages of this equation; it predicts a maximum value of the stress at high strains, when recovery dominates hardening (or the rate of dislocation annihilation becomes greater than the rate of dislocation multiplication). Simple power expressions predict ever increasing stresses and are therefore not realistic at high strains. The yield stress was taken as 100 MPa. This represents the yield stress for a polycrystal with large grain size. The saturation stress was taken from Table 1, where it corresponds to σ_{fGB}; this value of 900 MPa represents the maximum strength of copper, achievable only for very small grain sizes. This stratagem enables the simulation of the higher rate of hardening taking place at the grain boundaries. Four curves are shown in Fig. 9(b); they represent four work hardening rates. The curve with ε_c=0.01 was chosen for the computations. This was done in order to obtain a good fit with the experimental results. It is recognized that other parameters could also be varied. For instance, the saturation stress could be considered to vary with grain size. However, our knowledge of the evolution of the mechanical response of the grain boundary is not sufficient to add this additional variable to the model.

These different stress–strain responses were incorporated into the code Raven and calculations were successfully carried out. The results of one calculation for a grain size of 1 μm are shown in Fig. 10. The results are presented at three levels of the equivalent (effective) strain; 0.003, 0.01, and 0.55. The

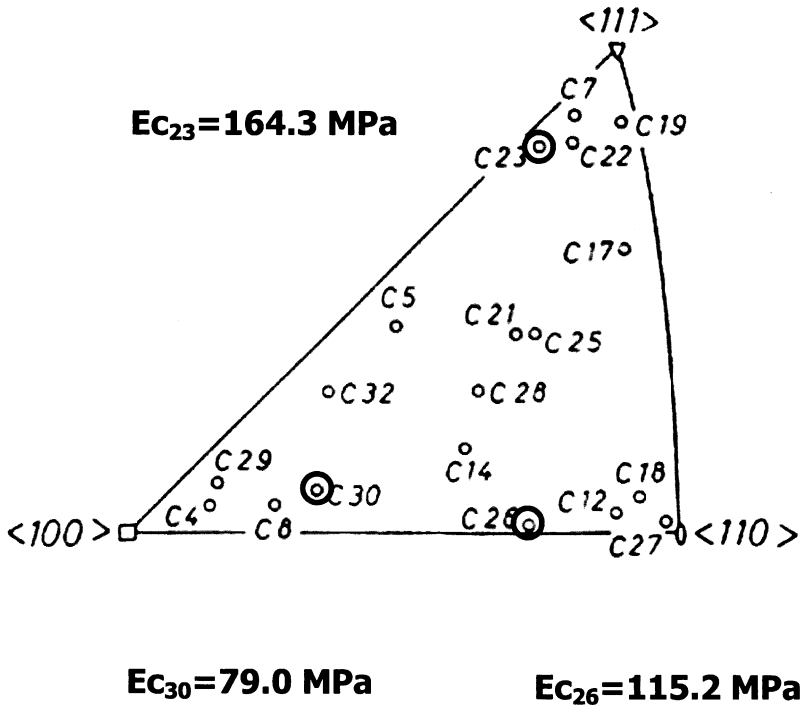

Fig. 8. Three crystallograghic orientations (marked by double circles) considered in computations (Experimental results from Diehl [52]); notice the equivalent isotropic elastic moduli marked for each orientation. The denominations C_{23}, C_{26}, and C_{30} are from Diehl [52].

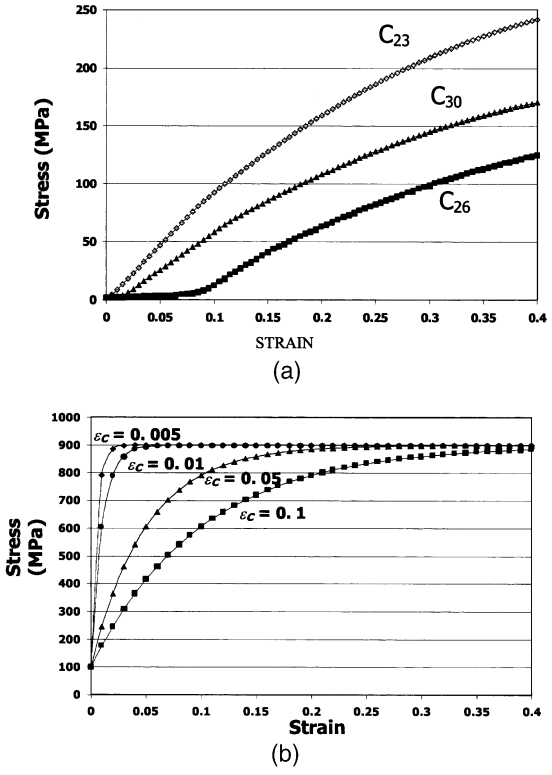

Fig. 9. (a) Plastic behavior of the grain interior: three grain orientations were taken from Diehl [52] curves extended using data by Suzuki *et al*. [53]; (b) Grain-boundary region, modeled by Voce equation.

evolution of strain can be clearly followed in the sequence shown in Fig. 9(b), (c), and (d). The strains are considerably higher in the grain interiors than in the grain boundary regions. Conversely, the stresses (not shown) rise rapidly in the grain-boundary region, while they remain low in the grain interiors. This is the direct result of the differences in constitutive response. Figure 11 shows a similar pattern for a grain size of 0.1 μm. Again, the strains are higher in the grain interiors. The computed stress–strain curves for grain sizes varying between 100 and 0.026 μm are shown in Fig. 12. The dramatic grain size dependence of this response is clearly demonstrated. The work hardening rate decreases as the grain size is decreased, while the flow stress increases. Experimental results are shown in the same plot, for comparison. The results by Andrade [56] for grain sizes of 117 and 9.5 m are in good agreement with the computed predictions. They show similar evolution in hardening. The computed results exhibit a higher sensitivity to grain size and it is possible that these predictions are more correct than the measurements. For D=26 nm, the match between the computed results and the experimental measurements by Weertman *et al*. [21] is excellent. The predictions were made using the grain-boundary thickness t given by equation (29), a slight deviation from the 1/2 exponent postulated in Section 3.

The presentation of the results in the Hall–Petch format enables a good evaluation of predictions; this is done in Fig. 13. The conventional Hall–Petch

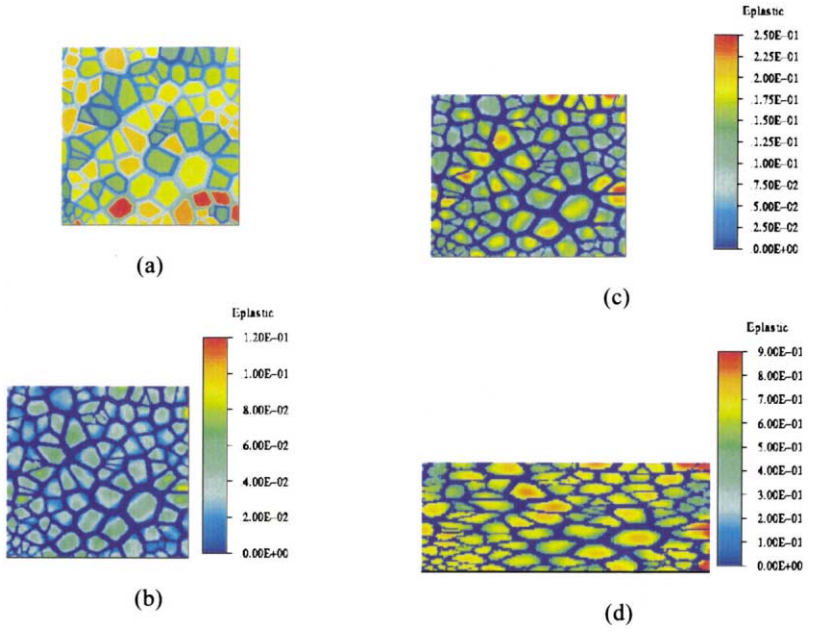

Fig. 10. Computation of plastic strains in 1 μm grain size; (a) initial grain configuration; (b,c,d) configurations with strain fields for specimen deformed to equivalent strains of 0.003, 0.01, and 0.55.

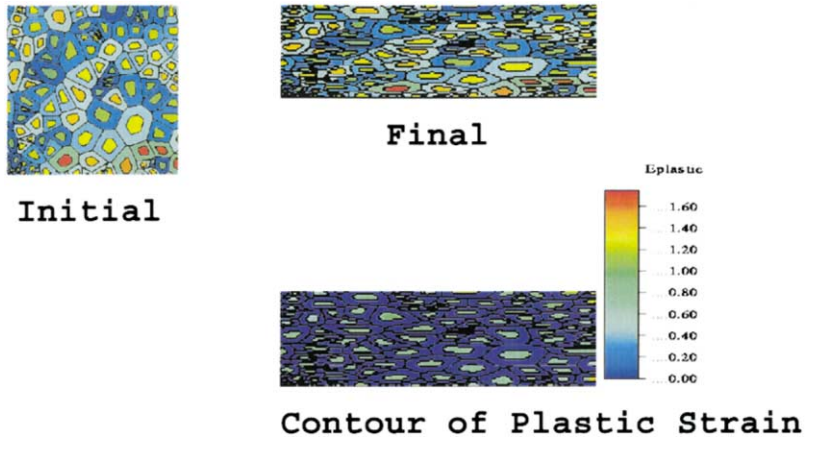

Fig. 11. The initial and final state with contours of the equivalent plastic strain for the microstructure with the 0.1 μm grain size. Plastic deformation distribution showing greater strain in grain interiors.

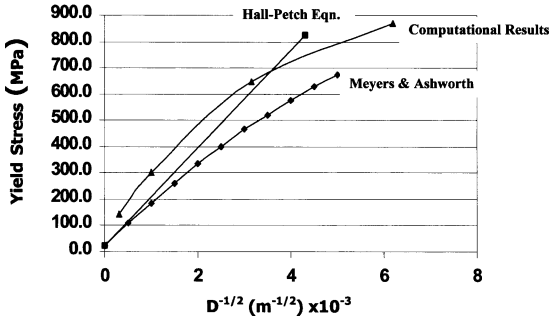

Fig. 12. Calculated and experimentally determined stress–strain curves for grain sizes ranging from 26 nm to 100 m.

response, obtained experimentally for larger grain sizes, is shown by a straight line. Both the analytical predictions from the Meyers–Ashworth equation and from the computations show a decrease in slope for the smaller grain sizes. This is significant. The computed yield stresses are higher than the ones analytically calculated because they are taken at a strain of 0.05. This was done because the elasto-plastic transition is not very clear in the computed stress–strain curves.

6. CONTRIBUTION DUE TO GRAIN-BOUNDARY SLIDING

Since a preliminary version of this computational procedure was introduced [57], there have been

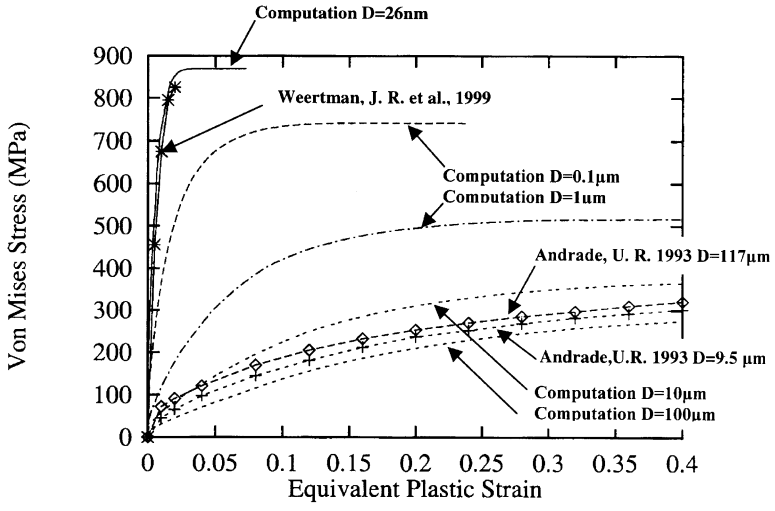

Fig. 13. Hall–Petch plot of yield stress variation with grain size $D^{-1/2}$ for copper; analytically calculated (M and A), computed, and Hall–Petch experimental results for large grain sizes presented in same figure. Notice decrease in slope at smaller grain sizes for M and A equation and computations.

strong recent suggestions that grain-boundary sliding can have a significant effect on the mechanical response of nanocrystals. Van Swygenhoven *et al.* [58] carried out molecular dynamics simulations that revealed sliding aliong boundaries. Kim *et al.* [59] proposed a composite model, into which they incorporated contributions of lattice and boundary diffusion. Conrad and Narayan [60] proposed a thermally-activated grain-boundary shearing mechanism. Both Kim *et al.* [59] and Conrad and Narayan [60] predict that sliding mechanisms become important for grain sizes on the order of nanometers, for copper. An important consideration in grain-boundary sliding not discussed in these previous calculations is the compatibility of deformation. Grain-boundary sliding can be represented by a viscous and a plastic accommodation term:

$$\tau_a = (\eta_i + \eta_D)\dot{\gamma} + \tau_p \tag{31}$$

where is the shear stress, η_{i} is an intrinsic grain-boundary viscosity, η_{D} is a diffusional component of the accommodation process, and τ_p is a plastic deformation term. Figure 14 shows an idealized polycrystal subjected to a shear stress τ_a. The intergranular sliding path is also shown. There is a need for accommodation, since sliding in polycrystals is not fully compatible; this is shown by the jagged grain-boundary sliding path in Fig. 14(a). Raj and Ashby [61] treated grain-boundary sliding in their classic 1971 paper. They considered the plastic accommodation between adjacent grains to occur by diffusion alone. Whereas Fig. 14(b) shows the grain-boundary sliding path, Fig. 14(c) shows the sinusoidal shape assumed in the Raj and Ashby [61] calculations. Taking both grain-boundary and bulk diffusion into consideration, they obtained the following expression for the sliding rate, $\dot{u}$:

$$\dot{u} = \frac{du}{dt} = \frac{2}{\pi}\frac{\tau_a \Omega}{kT}\frac{\lambda}{h^2} D_V \left(1 + \frac{\pi\delta}{\lambda}\frac{D_B}{D_V}\right) \tag{32}$$

The parameters λ and h define the sinusoidal boundary in Fig. 14(c) (wavelength and amplitude respectively); Ω is the atomic volume; δ is the thickness of the boundary; D_V and D_B are the volume and boundary diffusion coefficients respectively. At temperatures significantly below $T_m/2, D_B >> D_V$, and

$$\frac{\pi\delta}{\lambda}\frac{D_B}{D_V} \gg 1$$

Thus:

$$\dot{u} \approx \frac{2\delta\Omega D_B}{kT}\tau_a\left(\frac{1}{h^2}\right) \tag{33}$$

If it is assumed that each grain boundary layer will generate an identical sliding rate, a strain rate can be defined as:

$$\dot{\gamma} = \frac{\dot{u}}{2h} = \frac{\delta\Omega D_B}{kT}\tau_a\left(\frac{1}{h^3}\right) \tag{34}$$

The amplitude of the sinusoidal wave can be taken as $D/4$. Thus:

$$\dot{\gamma} = \frac{64\delta\Omega D_B}{kT}\left(\frac{1}{D^3}\right)\tau_a \tag{35}$$

For a constant amplitude and grain size, a number of parameters can be grouped and equation (35) can be expressed as:

$$\dot{\gamma} = \left(\frac{1}{\eta_e}\right)\tau_a \tag{36}$$

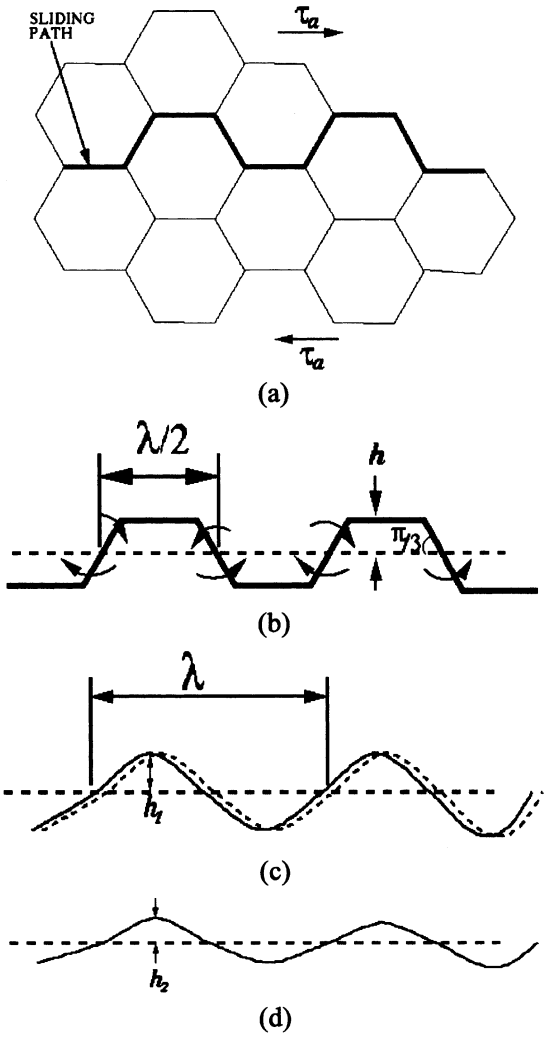

Fig. 14. (a) Schematic representation of grain-boundary sliding in polycrystal; (b) grain-boundary sliding path; (c) idealized sinusoidal path with diffusional migration of boundary according to Raj and Ashby [61]; (d) decrease in wave amplitude h with increasing plastic strain.

η_e is an effective viscosity. This is the equation for Newtonian viscous flow. The dependence of $\dot{\gamma}$ on h, in equation (34), is a clear suggestion that deformation will localize as h decreases. As plastic deformation proceeds, it is easily visualized how the jaggedness of the interface, measured by h, decreases. This is shown in the transition from Fig. 14(c) to (d). In nanocrystalline materials the flow localization, in the form of shear bands, is indeed observed [63–65].

Figure 15 shows a plot of $\dot{\gamma}$, calculated from the diffusional Raj and Ashby equation (equation (35)) as a function of grain size D. The stress levels were varied and are obtained from the compressive flow stresses for the various grain sizes calculated from the computational procedure presented in Section 5. They vary from 100 to 900 MPa, for grain sizes of 100 m to 26 nm, respectively. These stresses are converted

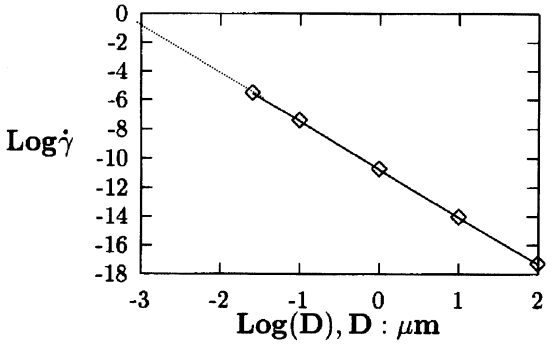

Fig. 15. Calculated strain rates from diffusionally-driven grain-boundary sliding as a function of grain size (copper deformed at 300 K); extrapolated results indicated by dashed line.

into shear stresses assuming a von Mises criterion (dividing them by $\sqrt{3}$). The values of the other parameters are: (~3b)=0.75 nm [60]; =0.0087 nm^3(=4/3 ^3r, r being the atomic radius for copper); T=298 K. The grain-boundary diffusion coefficient room temperature was taken as D_B=10^{-21} m^2/s at T/T_m=0.225. This value is higher than the extrapolation from Shewmon [62] (10^{-22}m^2/s) and lower than the one used by Kim *et al.* [59] (2.6×10^{-20}m^2/s). The five calculated strain rates are marked on plot and the data are well represented by a straight line. Extrapolation to smaller grain sizes (shown by dashed line) reveals striking results: for $D\leq$10 nm, the strain rate due to diffusional sliding along grain boundaries by a Raj–Ashby mechanism can reach significant values ($\dot{\gamma}$ $\geqslant10^{-4}$s^{-1}). It should be pointed out that plastic flow, not considered by Raj and Ashby [61], can also assist in the accommodation process at these temperatures. This plastic flow component is indicated, in equation (30), by τ_p. Thus, it is concluded that grain-boundary sliding can contribute to the plastic deformation at grain sizes $D\leq$10 nm, corroborating recent calculations [58–60].

The computational approach implemented here [50] uses time-independent plasticity. Therefore, time-dependent phenomena such as thermal activation, grain-boundary sliding, and diffusional mechanisms are not taken into account. Computations were carried out for an ideal case where the material has zero grain-boundary viscosity. The free sliding along the boundaries was assumed, i.e., η_e=0. This assumption is rather drastic, but necessary due to the nature of the constitutive response (time independent) of the material assumed in the computations. Compatibility was maintained by plastic deformation, i.e., no voids were allowed to open up. The shear strength of the grain boundaries was assumed to be zero, while their tensile strength was unaltered. Thus, only plastic deformation inhibited the free flow of the grains. Figure 16 shows the distribution of plastic equivalent (effective) strain along a vertical line for the two cases of rigid boundaries and free sliding, computed for a grain size of 20 nm subjected to a global strain of 0.008. The strains are very uniform for the perfect

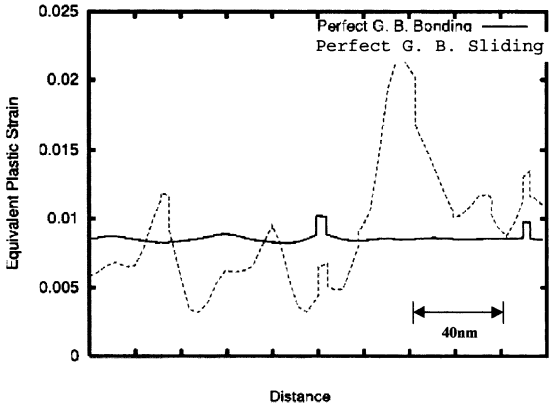

Fig. 16. Equivalent plastic strain as a function of distance from bottom boundary, along a vertical cutting plane (D=20 nm; ^{p}=0.008). Notice large much larger plastic strain variations for grain-boundary sliding case.

grain-boundary bonding situation, whereas the strain spikes are very noticeable for the grain-boundary sliding case. They correspond to localized sliding at the boundaries, which is accommodated by plastic deformation of the surrounding regions. The stress–strain curves are shown in Fig. 17. The resistance to plastic flow of the perfect sliding case represents the plastic accommodation of the grains required in sliding. This is a very significant component of the overall strength. Figure 18 shows the evolution in the distribution of plastic strains for the two cases, as the applied deformation is increased; three equivalent (compressive) plastic strains are shown: 0.007, 0.1, and 0.2.There is a much greater tendency for localization when the grain boundaries are allowed to slide. Indeed, shear localization is an important feature of the plastic deformation of nanocrystalline materials [63–65]. It should be pointed out that the rapid work hardening of the grain-boundary region, described by the Voce equation, is also a predisposing factor for shear localization in the nanocrystalline domain (where this response dominates). Although these results are preliminary, they indicate the importance of grain-boundary processes in the resistance to plastic deformation, global distribution of deformation and evolution of localization.

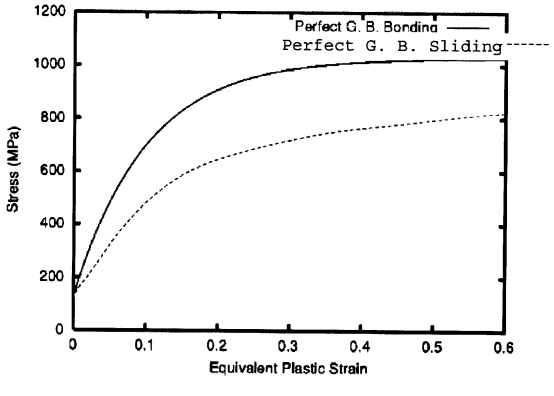

Fig. 17. Computed stress versus equivalent plastic strain (D=20 nm) for perfect grain-boundary bonding and free slip (no grain-boundary separation allowed).

7. CONCLUSIONS

It is proposed that elastic anisotropic effects, grain boundary sources, and the activation of two or more slip systems in polycrystals are responsible for the formation of a work hardened layer along the grain boundaries, early in the microplastic region. This grain boundary work-hardened layer becomes increasingly important as the grain size is decreased. Polycrystals are modeled (both analytically and computationally) as a composite of a work-hardened boundary layer surrounding grain interiors comprised of an annealed material having an essentially monocrystalline response. The analytical predictions using this framework are successfully extended from the micro to the nanocrystalline domain and show a good correlation with experimental results for copper and iron. The decrease of the Hall–Petch slope in the nanocrystalline domain is captured and corresponds to a grain size for which the thickness of the work hardened layer is equal to one half the grain diameter. Computational calculations using the Eulerian code Raven successfully produce stress–strain curves of the polycrystalline aggregates and indicate the correct trend in grain sizes as well as the decrease in the Hall–Petch slope as the grain size is decreased. The computations reveal the initiation and evolution of shear localization for the smaller grain sizes, in agreement with experimental results of Weertman *et al.* [20, 21] and Mallow and Koch [27–29], which report this effect.

The formation of this grain-boundary work hardened layer is discussed in terms of the statistically stored and geometrically necessary dislocations which are the physical foundation of strain-gradient plasticity theory. A slightly modified, alternative approach, is presented.

The importance of grain-boundary sliding in the nanocrystalline regime is discussed and it is shown that sliding can lead to a greater predisposition for shear localization, recently observed [63–65]. This is shown computationally; additionally, the Raj–Ashby approach, which considers exclusively diffusionally-driven sliding, is also discussed in the context of nanocrystalline polycrystal deformation.

Acknowledgements—This research was supported by the US Army Research Office Multidisciplinary University Research Initiative (Contract No. DAAH 04-96-1-0376) and NSF grant (DMI-9612017). The competent help of Mr. Sébastien Thillay was greatly appreciated. Prof. V. Lubarda revised the manuscript and provided many valuable insights. Discussions with Prof. R.J. Asaro and Dr. B.K. Kad are gratefully acknowledged.

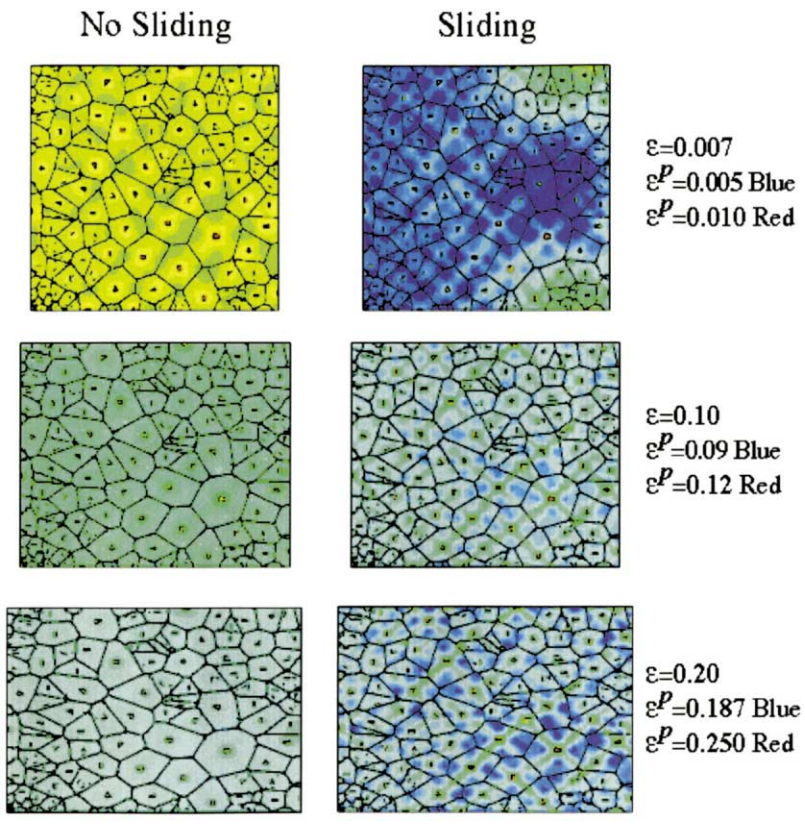

Fig. 18. Contours of equivalent plastic strain for perfect grain-boundary bonding (left) and free grain-boundary sliding (right) at effective strains of 0.007, 0.10, and 0.20).

REFERENCES

1. Hall, E. O., *Proc. Roy. Soc. (London)*, 1951, **B64**, 474.
2. Petch, N. J., *J. Iron Steel Inst.*, 1953, **174**, 25.
3. Conrad, H. and Schoeck, G., *Acta metall.*, 1960, **8**, 791.
4. Cottrell, A. H., *Trans. TMS-AIME*, 1958, **212**, 192.
5. Armstrong, R. W., in *Advances in Materials Research*, Vol. 4, ed. R. F. Bunshah. Wiley-Interscience, NY, 1971, p. 101.
6. Li, J. C. M., *Trans. TMS-AIME*, 1963, **227**, 75.
7. Conrad, H., *Acta Met.*, 1963, **11**, 75.
8. Ashby, M. F., *Phil. Mag.*, 1970, **21**, 399.
9. Hirth, J. P., *Met. Trans.*, 1972, **3**, 61.
10. Thompson, A. W., in *Work Hardening in Tension and Fatigue*, ed. A. W. Thompson. AIME, 1977, p. 399.
11. Murr, L. E. and Hecker, S. S., *Scripta metall.*, 1979, **13**, 667.
12. Suits, J. C. and Chalmers, B., *Acta metall.*, 1961, **12**, 854.
13. Worthington, P. J. and Smith, E., *Acta metall.*, 1964, **12**, 1277.
14. Margolin, H. and Stanescu, M. S., *Acta metall.*, 1975, **23**, 1141.
15. Meyers, M. A. and Ashworth, E., *Phil. Mag. A*, 1982, **46**, 737.
16. Birringer, R., Gleiter, H., Klein, H. -P. and Marquardt, P., *Phys. Lett.*, 1984, **102A**, 365.
17. Gleiter, H., *Z. Metallk.*, 1995, **86**, 78.
18. Nieman, G. W., Weertman, J. R. and Siegel, R. W., *Scripta metall. mater.*, 1990, **24**, 145.
19. Nieman, G. W., Weertman, J. R. and Siegel, R. W., *J. of Mat. Res.*, 1991, **6**, 1012.
20. Weertman, J. R., *Mat. Sci. and Eng.*, 1993, **A166**, 161.
21. Weertman, J. R., Farkas, D., Hemker, K., Kung, H., Mayo, M., Mitra, R. and Van Swygenhoven, H., *MRS Bulletin*, 1999, **24**, 44.
22. Armstrong, R. W. and Smith, T. R., in *Processing and Properties of Nanocrystalline Materials*, ed. C. Suryanarayana. PA, 1996, p. 345.
23. Pande, C. S., Masamura, R. A. and Armstrong, R. W., *Nanostr. Mat.*, 1993, **2**, 323.
24. Smith, T. R., Armstrong, R. W., Hazzledine, P. M., Masamura, R. A. and Pande, C. S., in *Pile-up Based Hall–Petch Considerations at Ultrafine Grain Sizes*, MRS, Boston, MA, 1995, p. 31.
25. Jang, J. S. C. and Koch, C. C., *Scripta mater.*, 1990, **24**, 1599.
26. Scattergood, R. O. and Koch, C. C., *Scripta metall.*, 1992, **27**, 1195.
27. Mallow, T. R. and Koch, C. C., *Acta mater.*, 1997, **45**, 2177.
28. Mallow, T. R. and Koch, C. C., *Met. and Mat. Trans.*, 1998, **29A**, 2285.
29. Koch, C. C., Morris, D. G., Lu, K. and Inoue, A., *MRS Bulletin*, 1999, **24**(2), 55.
30. Chokshi, A. H., Rosen, A. S., Karch, J. and Gleiter, H., *Scripta metall.*, 1989, **23**, 1679.
31. Aifantis, E. C., *Intl. J. Plasticity*, 1987, **3**, 211.
32. Fleck, N. A. and Hutchinson, J. W., *J. Mech. Phys. Sol.*, 1993, **41**, 1825.
33. Fleck, N. A., Muller, G. M., Ashby, M. F. and Hutchinson, J. W., *Acta metall. mater.*, 1994, **42**, 475.
34. Gao, H., Huang, J. Y., Nix, W. D. and Hutchinson, J. W., *J. Mech. Phys. Sol.*, 1999, **47**, 1239.
35. Gao, H., Huang, J. Y., Nix, W. D. and Hutchinson, J. W., *Mech. Phys. Sol.*, 2000, **48**, 99.
36. Ghahremani, F., Hutchinson, J. W. and Tvergaard, V., *J. Am. Cer. Soc.*, 1990, **73**, 1548.
37. Ghahremani, F. and Shih, C. F., *J. Appl. Mech.*, 1992, **59**, 61.
38. Margolin, H., *Acta mater.*, 1998, **46**, 6305.

39. Li, J. C. M. and Chou, Y. T., *Met. Trans.*, 1970, **1**, 1145.
40. Murr, L. E., *Interfacial Phenomena in Metals and Alloys*. Addison Wesley, Reading, MA, 1975.
41. Sutton, A. P. and Baluffi, R. F., *Interfaces in Crystalline Materials*. Oxford Univ. Press, NY, 1994.
42. Delaire, F., Raphanel, J. L. and Rey, C., *Acta mater.*, 2000, **48**, 1075.
43. Gray III, G. T., Chen, S. R. and Vecchio, K. S., *Met. and Mat. Trans.*, 1999, **30A**, 1235.
44. Adams, B. L and King, W. E., *Phyl. Mag., A*, 2000, **80**, 9.
45. Klepaczko, J., in *Impact Loading and Dynamic Behavior of Materials*, eds. C. Y. Chiem, H.-D. Kunze and L. W. Meyer. DGM, Oberursel, Germany, 1987, p. 823.
46. Feltham, P. and Meakin, J. D., *Phil. Mag.*, 1957, **2**, 105.
47. Meyers, M. A., de Andrade, U. R. and Chokshi, A. H., *Met and Mat. Trans.*, 1995, **26A**, 2881.
48. Abrahamson II, E. P., in *Surfaces and Interfaces*, Syracuse Univ. Press, 1968, p. 262.
49. Gertsman, V. Y., Hoffmann, M., Gleiter, H. and Birringer, R., *Acta mater.*, 1994, **42**, 3539.
50. Benson, D. J., *Comp. Meth. Appl. Mech. Engng.*, 1992, **99**, 235.
51. Van Leer, B., *J. Comp. Phys.*, 1977, **23**, 276.
52. Diehl, J., *Z. Metallk.*, 1956, **47**, 331.
53. Suzuki, H., Ikeda, T. and Takeuchi, T., *J. Phys. Soc. Japan*, 1956, **1**, 382.
54. Voce, E., *Metallurgia*, 1955, **51**, 219.
55. Kocks, U. F., *Trans. ASME*, 1976, **98**(1), 76.
56. Andrade, U. R., *Ph.D. Dissertation*, UCSD, 1993.
57. Meyers, M. A., Benson, D. J., and Fu, H.-H., in *Advanced Materials for the 21st Century*, eds. Y.-W. Chung, D. C. Dunand, P. K. Liaw, and G. B. Olson. TMS-AIME, Warrendale, PA, 1999, 499.
58. Van Swygenhoven, H., Spaczer, M. and Caro, A., *Acta mater.*, 1999, **47**, 561.
59. Kim, H. S., Estrin, Y. and Bush, M. B., *Acta mater.*, 2000, **48**, 493.
60. Conrad, H. and Narayan, J., *Scripta mater.*, 2000, **42**, 1025.
61. Raj, R. and Ashby, M. F., *Met. Trans.*, 1971, **2A**, 1113.
62. Shewmon, P. G., *Diffusion in Solids, 2nd Edn*. TMS-AIME, Warrendale, PA, 1989, p. 31, p. 200.
63. Zhu, X. H., Carsley, J. E., Milligan, W. W. and Aifantis, E. C., *Scripta mater.*, 1997, **36**, 721.
64. Sanders, P. G., Eastman, J. A. and Wertman, J. R., *Acta mater.*, 1997, **45**, 4019.
65. Mallow, T. R. and Koch, C. C., *Acta mater.*, 1998, **46**, 6459.